

# Modeling the GRB jet properties with 3D general relativistic simulations of magnetically arrested accretion flows

BESTIN JAMES,<sup>1</sup> AGNIESZKA JANIUK,<sup>1</sup> AND FATEMEH HOSSEIN NOURI<sup>1</sup>

<sup>1</sup>*Center for Theoretical Physics, Polish Academy of Sciences, Al. Lotników 32/46, 02-668 Warsaw, Poland*

## ABSTRACT

We investigate the dependence of the GRB jet structure and its evolution on the properties of the accreting torus in the central engine. Our models numerically evolve the accretion disk around a Kerr black hole using 3D general relativistic magnetohydrodynamic simulations. We use two different analytical hydrodynamical models of the accretion disk, based on the Fishbone-Moncrief and Chakrabarti solutions, as our initial states for the structure of the collapsar disk and the remnant after a binary neutron star merger, respectively. We impose poloidal magnetic fields of two different geometries upon the initial stable solutions. We study the formation and evolution of the magnetically arrested disk state and its effect on the properties of the emitted jet. The jets produced in our models are structured and have a relatively hollow core and reach higher Lorentz factors at an angle  $\gtrsim 9^\circ$  from the axis. The jet in our short GRB model has an opening angle of up to  $\sim 25^\circ$  while our long GRB engine produces a narrower jet, of up to  $\sim 11^\circ$ . We also study the time variability of the jets and provide an estimate of the minimum variability timescale in our models. The application of our models to the GRB jets in the binary neutron star post-merger system and to the ultra-relativistic jets launched from collapsing stars are briefly discussed.

**Keywords:** accretion, accretion disks, black hole physics, gamma-ray bursts, hydrodynamics, jets, MHD, magnetic fields, magnetohydrodynamical simulations, relativistic jets

## 1. INTRODUCTION

Gamma-ray bursts (GRBs) are transient phenomena observed in the high energy sky at cosmological distances. The emission of high energy photons is released at the jet photosphere and presents non-thermal spectral distribution (Piran 2004). Their bi-modal duration distribution suggests separate classes of progenitors being responsible for short and long events (Kouveliotou et al. 1993). The first class, long gamma ray bursts, have been identified with bright supernovae already in 1990s, e.g. for GRB 980425 (Galama et al. 1999). According to the collapsar model (Woosley 1993) the jet emerges after the collapse of a massive, rotating star and formation of a black hole in its core. The accompanying explosion gives supernova-like signatures in the emission spectra, up to several weeks after the GRB. The second class of bursts, whose duration is typically below couple of seconds, originates from compact binary merger events. Here the central compact object remnant is surrounded by an accretion disk that is created from remnant matter of a tidally

disrupted neutron star (Duez 2010). As a result, a Poynting-flux dominated jet can be generated self-consistently as part of the magnetohydrodynamic processes in the merger (Rezzolla et al. 2011; Ruiz et al. 2020). A confirmation of this type of progenitor came recently with the discovery of gravitational wave event GW170817 associated with short GRB of duration 1.7 seconds in its prompt phase (Abbott et al. 2017). The accompanying observations showed clearly the multi-messenger characteristics of this object (Margutti & Chornock 2021).

GRBs are seen as relativistic jets pointing towards our line of sight, when observed from Earth. Relativistic jets are ubiquitous phenomena in many accreting black hole sources. It is widely assumed that the properties of the accretion inflow affect the properties of the jet. The process which is responsible for driving accretion in magnetized disks is considered to be the magnetorotational instability (MRI) as described by Balbus & Hawley (1991). The formation of the magnetically arrested disk (MAD) has been invoked recently to explain the properties of the jets observed (see Abramowicz & Fragile (2013) for a review). In such scenarios a large scale bipolar field is accumulated around the central object due to the inward accretion of the plasma. Such a large-scale field is unable to dissipate locally by the magnetic diffusivity, unlike a

small-scale field, and cannot be absorbed if the central object is a black hole. The field thus accumulates in the innermost region of the accretion disk and results in the formation of a MAD (Narayan et al. 2003). In such a situation, the interchange instability comes into play subsiding the MRI which already should have developed initially due to the turbulence in the magnetized accretion flow (Proga & Zhang 2006). The accretion further proceeds in a MAD state mainly due to the interchange instability. The presence of large-scale bipolar fields in the accretion disks is often associated with the formation of astrophysical jets observed at various scales. Depending on the mass load, the magnetically driven jets can be classified into Poynting jets and hydromagnetic jets. The Poynting jets are naturally self-collimated and are powered either by the disks themselves or by the rotation of the black hole (Blandford & Znajek 1977; Li 2000). The existence of the MAD state can be linked to the production of powerful Poynting jets (Igumenshchev 2008). Tchekhovskoy et al. (2011) showed the formation of relativistic jet from a MAD state and the extraction of rotational energy of the black hole by the emitted jet according to the Blandford-Znajek mechanism. The other possible mechanism for jet launching in short GRBs is explained by neutrino-dominated accretion flows (NDAFs) (Popham et al. 1999; Di Matteo et al. 2002; Janiuk et al. 2004; Liu et al. 2017). Since the post-merger disks are transparent for neutrinos, NDAFs are cooled continuously by neutrino emissions. This scenario proposes that some emitted neutrino energy can be transferred to a pair fireball through neutrino-antineutrino annihilations to generate the collimated jets along the axis perpendicular to the disk plane (Paczynski 1991; Jaroszynski 1996; Richers et al. 2015; Just et al. 2016; Perego et al. 2017).

The MAD models have been studied previously to explain the jet formation and time variability's dependencies on black hole's spin (Narayan et al. 2021), and formation of the blazar gamma-ray flares in active galactic nuclei (AGNs) and supermassive black holes at the galaxy centers such as M87 (Mizuta et al. 2018; Chael et al. 2019). Liska et al. (2020) investigated the effects of the initial magnetic field configuration and White et al. (2019) performed numerical convergence studies of the MADs. Moreover, the MADs were applied in the context of the GRB observations explaining the variability of long GRB's luminosity during the prompt phase (Lloyd-Ronning et al. 2016), and constraining the magnetic field and black hole mass required to power Blandford-Znajek jets (Lloyd-Ronning et al. 2019).

In this article, we aim to explain the jet properties of long and short GRB engines considering a magnetically arrested disk as the central engine. We use the method of Janiuk et al. (2021) to determine the variability properties of these jets, extending now our previous work to the long-time, 3-dimensional simulation of MADs. We investigate the prop-

erties of the relativistic jets produced by an accreting system around a Kerr black hole with two different hydrodynamical models of the accretion disk, using 3-dimensional general relativistic magnetohydrodynamic (GRMHD) simulations. We impose the initial magnetic field configurations such that the inner region of the disk builds up a substantial amount of poloidal flux in a short amount of time. Our intention was to achieve the MAD state rather faster and to study the dependence of the jet properties on such a central engine configuration.

The article is organized in the following way. In Section 2 we present the numerical setup and initial configuration of our models. In Section 3 we describe the evolution of the disk, the formation of the MAD state, the properties of the resulting jet structure and some analysis of our results. The astrophysical implications of our models, the application of our results to the short and long GRBs and some further analysis are given in Section 4. Finally we give the conclusions in Section 5.

## 2. NUMERICAL SETUP AND MODELS

### 2.1. Code

We use our implementation of the GRMHD code HARM (Gammie et al. (2003), Noble et al. (2006), Sapountzis & Janiuk (2019)) for evolving our models in a fixed Kerr metric. It is a conservative and shock capturing scheme for evolving the equations of GRMHD. The code follows the flow evolution by numerically solving the continuity, energy-momentum conservation, and induction equations in the GRMHD scheme

$$\nabla_\mu(\rho u^\mu) = 0 \quad (1)$$

$$\nabla_\mu(T^{\mu\nu}) = 0 \quad (2)$$

$$\nabla_\mu(u^\nu b^\mu - u^\mu b^\nu) = 0 \quad (3)$$

Here,  $u^\mu$  is the four-velocity of the gas,  $u$  is the internal energy,  $\rho$  is the gas density,  $p$  is the gas pressure, and  $b^\mu$  is the magnetic four vector. The stress-energy tensor is comprised of the gas and electromagnetic parts:  $T^{\mu\nu} = T_{gas}^{\mu\nu} + T_{EM}^{\mu\nu}$  where,

$$T_{gas}^{\mu\nu} = \rho h u^\mu u^\nu + p g^{\mu\nu} = (\rho + u + p) u^\mu u^\nu + p g^{\mu\nu}, \quad (4)$$

$$T_{EM}^{\mu\nu} = b^2 u^\mu u^\nu + \frac{1}{2} b^2 g^{\mu\nu} - b^\mu b^\nu, b^\mu = u_\nu^* F^{\mu\nu} \quad (5)$$

Here,  $F$  is the Faraday tensor and in a force-free approximation, we have  $E_\nu = u^\nu F^{\mu\nu} = 0$ . We adopt dimensionless units in the code, with  $G = c = M = 1$  for our simulations. Thus the length in the code units is given by  $r_g = GM/c^2$  and

the time is given by  $t_g = GM/c^3$ , where  $M$  is the mass of the black hole. So our models can represent the central engines of both the short and long gamma ray bursts.

The initial equilibrium torus state is prescribed in the Boyer-Lindquist coordinates (Boyer & Lindquist (1967)) in the original solutions and they are transformed into Kerr-Schild (KS) coordinates in the code (see Weinberg (1972) & Visser (2007)). The integration is done in the code in modified Kerr-Schild coordinates. So in the code, the KS radius  $r$  has been replaced by a logarithmic radial coordinate  $x^{[1]}$  such that  $r = e^{x^{[1]}}$ , the KS latitude  $\theta$  has been replaced by  $x^{[2]}$  such that  $\theta = \pi x^{[2]} + \frac{(1-h)}{2} \sin(2\pi x^{[2]})$  and the azimuthal angle  $\phi$  remains the same,  $\phi = x^{[3]}$ . Here the parameter  $h$  can be adjusted to concentrate the numerical resolution near to the mid-plane and we use a value of 0.5 for it in our models.

## 2.2. Models

The initial state of our models is assumed to be a pressure equilibrium torus, which is embedded in a poloidal magnetic field. The Kerr black hole will accrete matter onto it due to the development of the MRI in the disk and this will in turn affect the evolution of magnetic field. Our models have a black hole spin characterized by the Kerr parameter  $a = 0.9$ . It is in the range of equilibrium spin values estimated by Gammie et al. (2004) for the models with stellar mass black holes. The simulations are run with a resolution of  $288 \times 256 \times 128$  in  $r$ ,  $\theta$ , and  $\phi$  directions, respectively. We use the  $\gamma$ -law equation of state  $p_g = (\gamma - 1)u$  in all our models, where  $p_g$  is the gas pressure,  $\rho$  is the gas density and  $u$  is the internal energy. We use a value of  $4/3$  for  $\gamma$ .

For our first model (FM76), the initial state of the accreting torus is prescribed according to Fishbone & Moncrief (1976) (hereafter FM) who gave an analytic solution of a constant angular momentum steady state. We specify the initial size of the torus in geometrical units where the its inner edge  $r_{in}$  is located at  $6r_g$  and the radius of pressure maximum  $r_{max}$  is located at  $13r_g$ . This solution corresponds to a constant specific angular momentum  $l = 7.414$  in the torus. For this model the outer edge of the disk is located around  $60 r_g$ . We embed this initial torus configuration in a poloidal magnetic field, where the field lines follow the isocontours of density (see the top left panel in Fig.1). For this field, the only non-zero component of the magnetic vector potential is given by

$$A_\phi(r, \theta) = r^5 (\rho_{avg} / \rho_{max}) - 0.2 \quad (6)$$

which has a dependence on the disk density structure as well as a power of radius. Here,  $\rho_{max}$  is the initial density maximum inside the torus and  $\rho_{avg}$  is the average of the density value from the adjacent cells in the computational grid. We choose this field configuration with the intention of eventually bringing a large poloidal flux to the vicinity of the black hole. We use the initial gas to magnetic pressure ratio,

$\beta = p_{gas} / p_{mag}$ , to normalize the magnetic field in the torus. Here  $p_{gas} = (\gamma - 1)u_{max}$  and  $p_{mag} = b_{max}^2 / 2$ , where  $u_{max}$  is the internal energy of the gas at the radius of maximum pressure. We normalize  $\beta$  to a value 100 at the radius of maximum gas pressure,  $r_{max}$  in the torus.

Our second hydrodynamical model (Ch85) of the accreting torus uses the Chakrabarti (1985) solution as the initial state. In this model the angular momentum has a power law relation along the radius with the von Zeipel parameter  $\lambda = (l/\Omega)^{1/2}$ , where  $l$  denotes the specific angular momentum and  $\Omega$  denotes the angular velocity. We adjust the size of the torus in the geometrical units using the parameters  $r_{in(vonZeipel)}$ , which is the true inner edge of the disk in this model, with a value of  $6r_g$  and the radius of pressure maximum  $r_{max}$  with a value of  $16.95r_g$ . We use different values here from that of the FM model, due to the different hydro-dynamical structure of the torus. The initial masses of the disks in both models are in the same range. The initial state of this model is shown in the left panel of the Figure 2. In this model the outer edge of the torus is located around  $80r_g$ . In order to compare the size of the disk in both the models, we calculate the total mass of the disk at the initial time. Using the appropriate density unit scaling, for the physical models we are considering, these values are estimated as  $0.925M_\odot$  and  $0.132M_\odot$  respectively for the FM and Chakrabarti solutions. In our scenario, these models represent separately the long and short GRB central engines. In our second model, we embed the initial torus configuration in a poloidal magnetic field. Here, the field is given as the magnetic field produced by a circular current. The only non-vanishing component of the vector potential in such a configuration is given by (e.g. in Jackson (1998)):

$$A_\phi(r, \theta) = A_0 \frac{(2 - k^2) K(k^2) - 2E(k^2)}{k\sqrt{4Rr\sin\theta}} \quad (7)$$

$$k = \sqrt{\frac{4Rr\sin\theta}{r^2 + R^2 + 2Rr\sin\theta}}$$

where  $E, K$  are the complete elliptic functions and  $A_0$  is a quantity which can be used to scale the magnetic field. In our model the radius of the circular wire  $R$  is taken as radius of pressure maximum  $r_{max}$  of the disk. We scale the magnetic field across the torus using the initial gas to magnetic pressure ratio,  $\beta = p_{gas} / p_{mag}$ . It has a maximum value of 480 inside the disk and has an average value of 100 within the disk. Therefore both our models are embedded in initial magnetic fields of comparable strength. The summary of initial parameters used in our models are given in Table 1.

In order to break the axisymmetry, we introduce a 2% amplitude random perturbation (as similar to Mizuta et al. (2018)) to the internal energy such that  $u = u_0(0.98 + 0.1X)$  where,  $u_0$  is the equilibrium internal energy in our models and  $X$  is a random number in the range  $0 \leq X \leq 1$ . This per-

Model	Initial magnetic field geometry	Kerr parameter ( $a$ )	Inner edge of the disk $r_{in}$ (in $r_g$ )	Radius of pressure maximum $r_{max}$ (in $r_g$ )	Mass of the disk in $M_\odot$	Initial $\beta$ in the disk
1. FM76	Poloidal field - following the disk density structure	0.90	6.0	13.0	0.925	100
2. Ch85	Poloidal field - due to a circular current at $r_{max}$	0.90	6.0	16.95	0.132	100

**Table 1.** The summary of initial parameters used in our models.

turbation breaks the initial axisymmetry of the system and helps in the development of non-axisymmetric modes.

### 3. RESULTS

#### 3.1. Initial configuration and evolution of the magnetized tori

We start our simulations with a stable equilibrium analytic torus solution, as described in the previous section. The imposed magnetic field on the initial stable configuration causes turbulence inside the plasma and results in the MRI. This acts as a mechanism which transports angular momentum outwards from the torus. Thus the matter starts to accrete into the black hole. The geometry of the imposed magnetic field has some pronounced effect on the further evolution of the system. In our first model, the imposed field is based on the magnetic vector potential which is dependent on the fifth power of the radius. So the poloidal field is smoothed out over a large distance and it takes a certain time for the plasma to bring the flux nearer to the black hole horizon. Such a configuration is plausible for collapsar central engines, where the core collapse leads to magnetic flux compression (e.g. Burrows et al. (2007), see also Tchekhovskoy et al. (2011)). On the other hand in our second model, the initial poloidal field is already strong near the horizon since it has the maximum value at the radius of pressure maximum ( $r_{max}$ ) of the disk. Such a configuration is adequate to describe the magnetic field in the post-merger remnant torus (see Paschalidis et al. (2013)).

The evolved states of the flow after some time has elapsed, illustrated by the density structure, are in the middle and right panels of the Figures 1 and 2, at times  $t = 2500 t_g$  and  $t = 5000 t_g$  respectively. The over-plotted lines show the magnetic field. It can be noticed that the initial conditions have relaxed and the accretion has started due to the action of the magnetic field. We observe a couple of azimuthal modes of the Rayleigh-Taylor instability developing in the turbulent region of the inner disk. Hence, the accretion is steadily driven and proceeds despite the formation of a magnetic barrier. When we plot the streamlines of velocity similarly at the same time instances, the velocity field lines loosely follow the structure of the density distribution inside the disk and along the equatorial region we can see the matter going in to the black hole. In the regions away from the disk, we observe outflows. In

the poloidal slices for the evolved stages, we observe that the velocity streamlines always point outward near to the polar axis from the black hole which show the direction of jet flows in the model.

In Figure 3 we show the evolution of the azimuthally averaged toroidal component of the magnetic field and its expansion with the polar angle ( $\theta$ ) over time. Initially, there is no magnetic field in the poles in either of the models, while the strong toroidal field is generated at the equatorial plane, in the accreting torus due to its differential rotation. The field is transported to the black hole horizon with the MRI turbulence and is present there shortly after the beginning of the simulation. The average shown in the plots is taken at  $\phi = (0, 2\pi)$  and at a radius of  $10 r_g$ . With time, the toroidal field develops also at polar regions, where it is being wind-up by the rotation of the black hole. It is also transported from the accretion disk towards the intermediate latitudes, via magnetic buoyancy, but in these regions the strength of the field is smaller than at the poles. In both our models we observe strips showing the periodic changes of the toroidal field component towards the polar regions. They seem to be anticorrelated with the pulses of poloidal magnetic field, depicted in Fig. 4, discussed below. In the second model, we notice also the field reversal in the regions near to the equator, which occurs predominantly at the initial period of the simulation ranging from time  $1500 t_g$  to  $6000 t_g$ . This is not noticed in our FM model evolution, however Mizuta et al. (2018) noted the field reversals also in their FM simulations, albeit with twice smaller resolution than in our models.

In Figure 4 we show the time evolution of the poloidal and toroidal components of the magnetic field in our models. The strength of the field components is calculated at the equator ( $\theta = \pi/2$ ) by averaging it over the whole range of  $\phi$  ( $0 \leq \phi \leq 2\pi$ ) and also averaged for the radius in the range  $r_{hor} \leq r \leq 10 r_g$ , where the magnetic field is mostly concentrated. The plots show that the initially imposed poloidal field gets amplified with time due to the turbulence in the plasma in both the models. It can also be observed that the toroidal component is initially zero but reaches a considerable strength (up to an order of  $\sim 10^{-2}$  in code units) over time due to the winding by the black hole rotation. The strength of the developed toroidal component remains higher in the disk than the poloidal counterpart for most of the simulation.



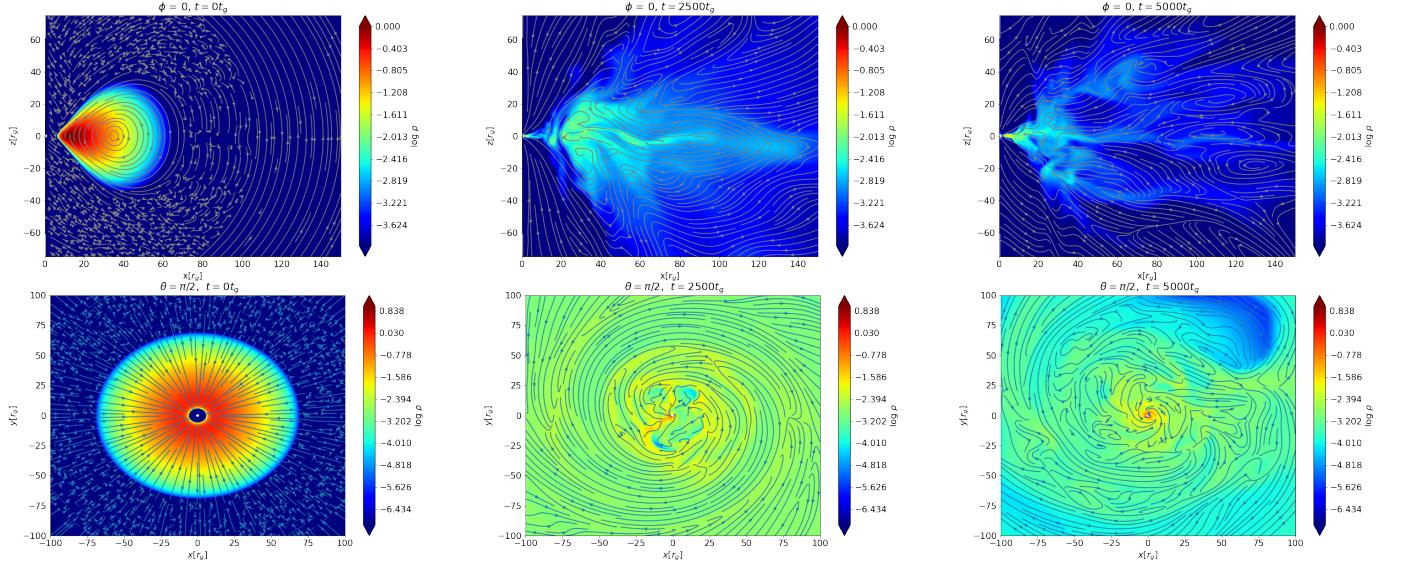


**Figure 1.** Snapshots of torus density structure along a poloidal plane ( $\phi = 0$  slice) (top panel) and along the equatorial plane ( $\theta = \pi/2$  slice) (bottom panel) with streamlines of magnetic field at  $t = 0$  (left), 2500 (middle) and 5000  $t_g$  (right), for the model with initial  $\beta = 100$  and Fishbone-Moncrief configuration with Kerr parameter  $a = 0.90$ .

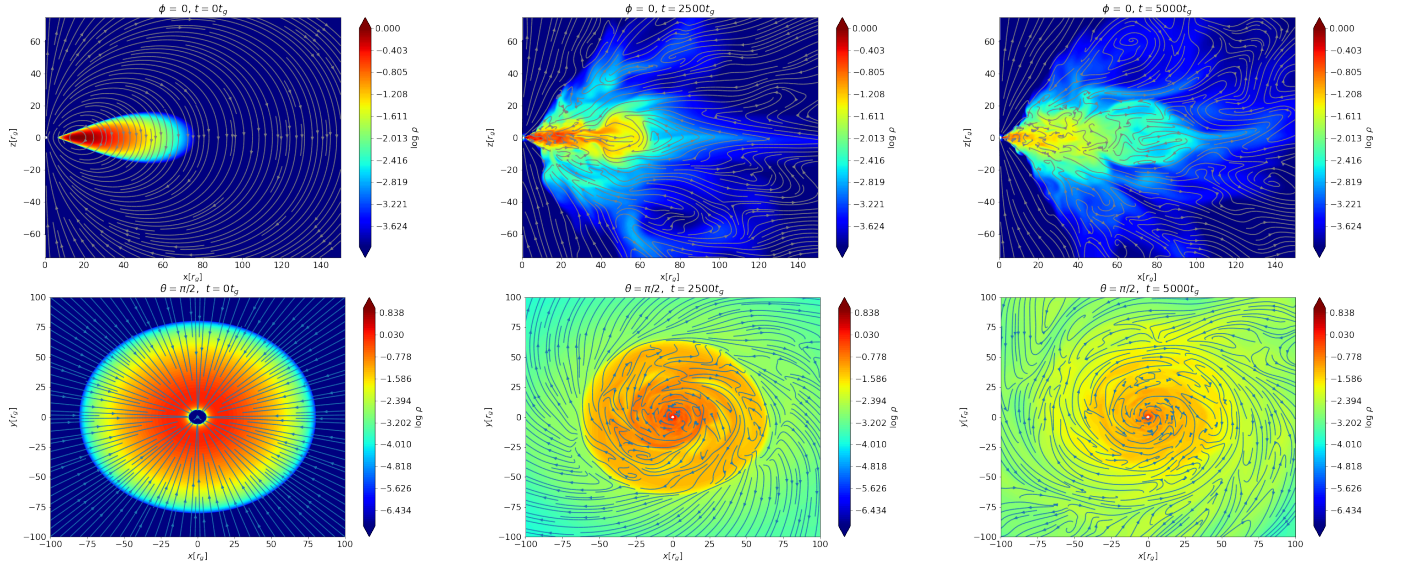


**Figure 2.** Snapshots of torus density structure along a poloidal plane ( $\phi = 0$  slice) (top panel) and along the equatorial plane ( $\theta = \pi/2$  slice) (bottom panel) with streamlines of magnetic field at  $t = 0$  (left), 2500 (middle) and 5000  $t_g$  (right), for the model with initial average  $\beta = 100$  and Chakrabarti configuration with Kerr parameter  $a = 0.90$ .

The jet is launched thanks to the development of the toroidal magnetic field, which also helps in collimation of the jet base, in addition to the ram pressure acting at larger scales.

In Figure 5 we show the mass accretion rate near the black hole horizon as a function of time for both our models. The accretion starts after a short amount of time due to the development of the magnetic turbulence. This brings in plasma to the black hole horizon along with the magnetic flux. The sudden increase in the accretion rate in the beginning of the simulation can be attributed to the development of the magnetic turbulence which begins to bring the matter in the disk

to the horizon and relaxation of the initial stationary conditions. But when a substantial amount of magnetic flux is built up near the horizon, the accretion significantly reduces shortly afterwards which can be seen as the sudden drop in the accretion rate after around 1500  $t_g$ . This trend is observed in both our models but is more pronounced in the second one due to the specific geometry of the initially applied field. This is connected to the formation of the magnetically arrested disk. Thus our second model reaches the magnetically arrested state much quicker than the first one. The mass accre-

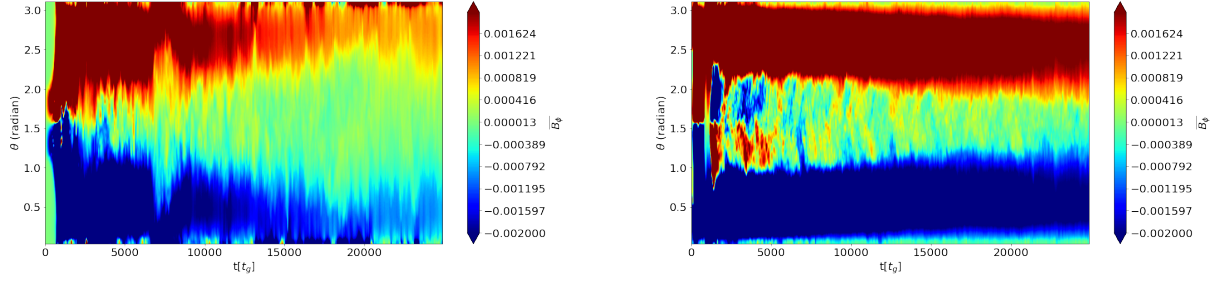


**Figure 3.** Butterfly diagram: showing the spatio-temporal evolution of the azimuthally averaged toroidal field  $\bar{B}_\Phi(r = 10r_g, \theta, t)$  in our models with (a) FM initial disk and (b) Chakrabarti initial disk configuration.

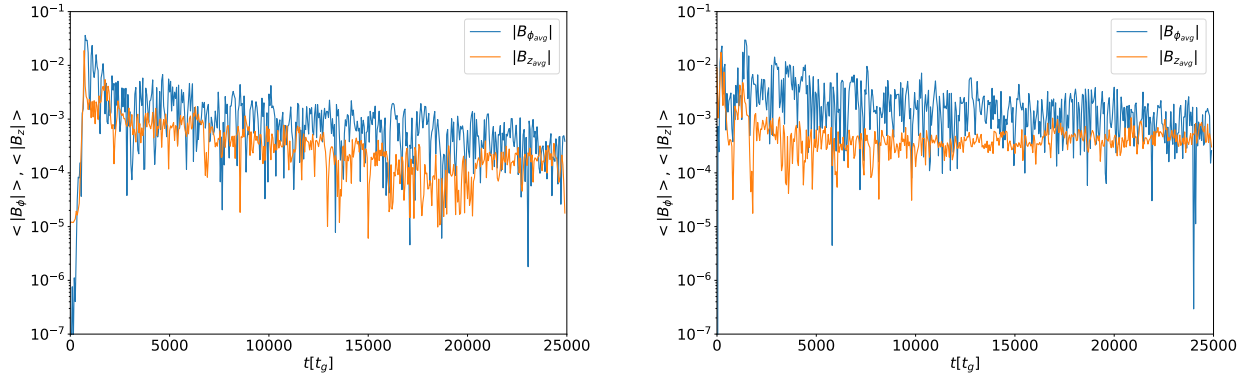


**Figure 4.** Strengths of the toroidal and poloidal components of the magnetic field at the equator ( $\theta = \pi/2$ ) averaged over  $r_{hor} \leq r \leq 10r_g$  and  $0 \leq \phi \leq 2\pi$ , with time (a) for model with initial Fishbone-Moncrief configuration (FM76) and (b) with initial Chakrabarti configuration (Ch85).

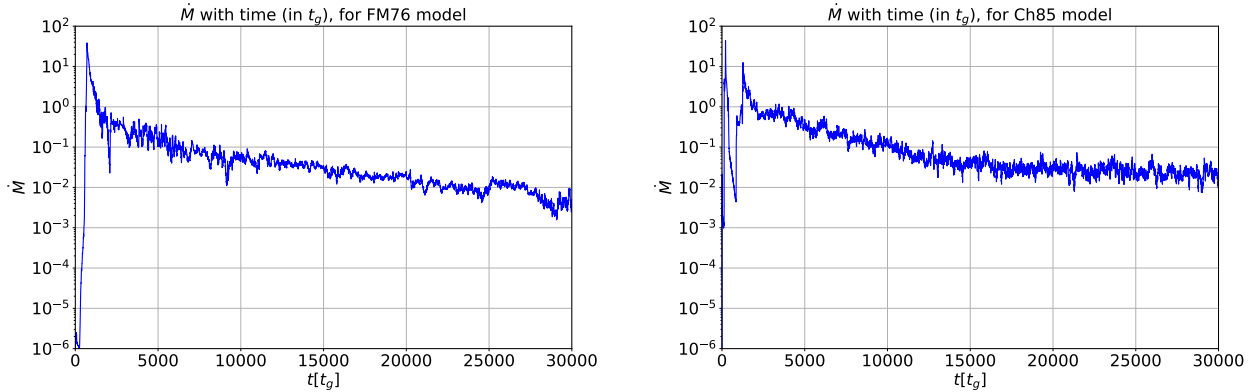


**Figure 5.** Mass accretion rate at the event horizon ( $\approx 1.4r_g$ ) with time (in  $t_g$ ) (a) for model with initial Fishbone-Moncrief configuration (FM76) and (b) with initial Chakrabarti configuration (Ch85).

tion proceeds and sustains in time due to the plasma instabilities further developed in the disk.

### 3.2. Formation of the magnetically arrested disk

In our simulations the accretion of matter onto the black hole is initiated due to the MRI and proceeds further due to the sustained turbulence in the plasma. Depending on the

initial geometry and strength of the magnetic field, it is probable that the accreting material brings a substantial amount of poloidal flux to the vicinity of the black hole over time. In such cases after a certain time, the strength of the magnetic field threading the black hole horizon increases considerably. A strong poloidal magnetic field developed in such a way will impede with the accretion and push away the plasma coming

into the black hole. Thus the smooth flow of matter along the equatorial axis is halted and the further accretion proceeds mainly in short episodes due to the interchange instability developed in the plasma afterwards. Such a state of the accreting torus is often called as the magnetically arrested disk (MAD) state. We observe the MAD state in both of our models with full 3D simulations. To parameterize the amount magnetic flux on the black horizon as compared to the inward flow of matter, we calculate the normalized and averaged magnetic flux threading each hemisphere of the black hole horizon. It is computed as

$$\phi_{BH}(t) = \frac{1}{2\sqrt{M}} \int_{\theta} \int_{\phi} |B^r(r_H, t)| dA_{\theta\phi} \quad (8)$$

The magnetic flux threading the black hole horizon, normalized to the mass flux, is shown in Figure 6 for both our models (In our code we use the Gaussian units and so a factor of  $4\pi$  is not included in this flux). It can be seen that our models have dynamically evolving magnetic fields in the inner disk region. In the model with FM initial configuration, we notice from the plot that the magnetic flux gets built up as the accretion proceeds, even though the initially applied field is not extremely strong, quantified by the plasma beta value as high as 100 inside the disk. After around 1000 dynamical times, the normalized magnetic flux reaches the highest value of up to 50. The mass inflow is thus hindered with due to the building up of the field and the disk reaches a magnetically arrested state. The mass accretion rate considerably reduces from above 10 to the range of  $10^{-1}$  to  $10^{-3}$  (in code units) after such a state is achieved (see Figure 5). This normalized magnetic flux on the horizon always remain 10 times or more larger than the mass flux as the model further evolves and the disk stays in a magnetically arrested configuration. In the model with the Chakrabarti initial state, we see such an effect more immediately after the accretion starts. The normalized magnetic flux threading the black hole horizon reaches the value of upto 120, as compared to the mass flux. This higher value as compared to the previous model can be attributed to the different initial magnetic field configuration we use in this model, even though the strengths are comparable. But here also, the accretion proceeds afterwards due to the instabilities developed in the plasma afterwards, especially due to the interchange instability. The magnetic flux normalized to the mass flux at the horizon remains higher than 20 in this model for most part of the simulation and has a more dynamic nature. The time averaged values of this magnetic flux at the horizon are 15.33 for the FM76 model and 25.49 for the Ch85 model, respectively.

### 3.3. Jet power and energetics

We use the jet energetics parameter  $\mu$  to estimate the Lorentz factor at infinity, assuming all energy is transformed

to the baryon bulk kinetic, as shown by Vlahakis & Königl (2003). It is defined as:

$$\mu = -\frac{T_t^r}{\rho u^r} \quad (9)$$

Here,  $T_t^r$  is the energy component of the energy-momentum tensor which comprises of matter and electromagnetic parts,  $\rho$  is the gas density and  $u^r$  is the radial velocity. So it is the total plasma energy flux normalized to the mass flux.

Figure 7 shows the structure of the jet by the distribution of the  $\mu$ -parameter at  $5000 t_g$  for both the models. We choose two locations along the jet direction and estimate the value of the jet energetic parameter  $\mu$  at these locations. The chosen location 1 is at  $r = 150 r_g$ ,  $\theta = 5^\circ$  which is in the inner region of the jet close the polar axis while the location 2 is at  $r = 150 r_g$ ,  $\theta = 10^\circ$  which is towards the outer region of the jet. The values we get from these locations are averaged over the whole toroidal angle  $\phi$ . We calculate the Lorentz factor of the observed jets from our models as the time average of  $\mu$  (after the jet has launched) at these chosen locations. The Lorentz factor averaged from the two locations for the FM model is 97.71 and for the Chakrabarti model is 131.85. So both the jets are accelerated to high relativistic velocities. The higher Lorentz factor in the second model may be attributed to the different initial structure of the magnetic field, which extends beyond the disk.

The time variability of the jet referring to the jet energetic parameter  $\mu$  is discussed in the next subsection.

In order to estimate the Blandford-Znajek luminosity of the emitted jet, we compute the radial energy flux by (see McKinney & Gammie (2004))

$$\dot{E} \equiv \int_0^{2\pi} \int_0^\pi d\theta d\phi \sqrt{-g} F_E \quad (10)$$

where  $F_E \equiv -T_t^r$ . This can be further subdivided into matter  $F_E^{(MA)}$  and electromagnetic  $F_E^{(EM)}$  parts. The electromagnetic part, only which we consider in our computation above, is given by (see McKinney et al. (2012))

$$T^{(EM)\mu}_{\nu} = b^2 u^\mu u_\nu + p_b \delta^\mu_\nu - b^\mu b_\nu \quad (11)$$

We show the evolution of the jet power with time estimated from the Blandford-Znajek luminosity in Figure 8. Notice that the plots are also marked with physical units assuming a central black mass of  $3 M_\odot$  for the short GRB central engine and a mass of  $10 M_\odot$  for the long GRB progenitor central engine (see Sharma et al. (2021) for an estimated range of black hole masses for observed GRB samples). It can be noticed from the plots that the jet power rises after a certain amount of time after the simulations have begun; the jet formation time is actually coincident with the development



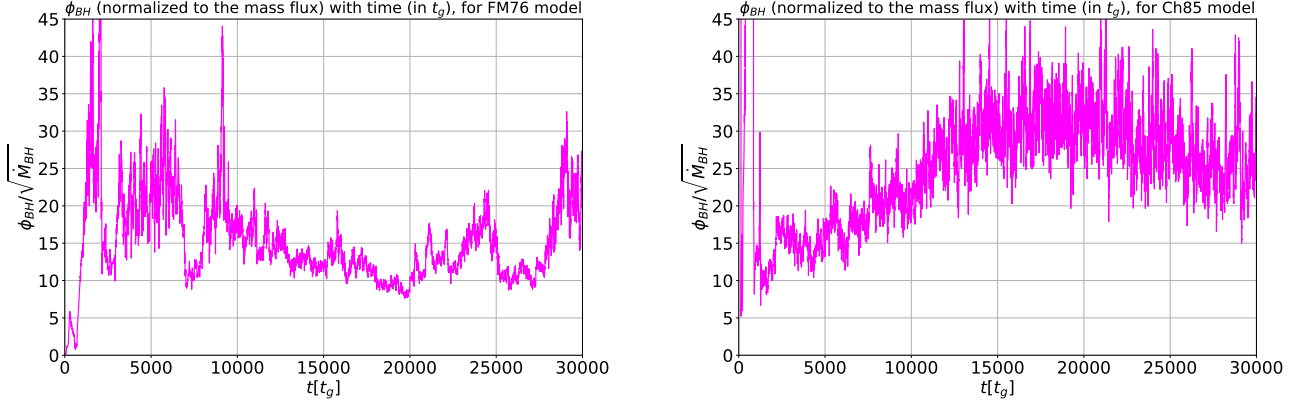


**Figure 6.** Time evolution of the magnetic flux on the black hole horizon normalized to the mass flux (a) with initial Fishbone-Moncrief configuration (FM76) and (b) with initial Chakrabarti configuration (Ch85).

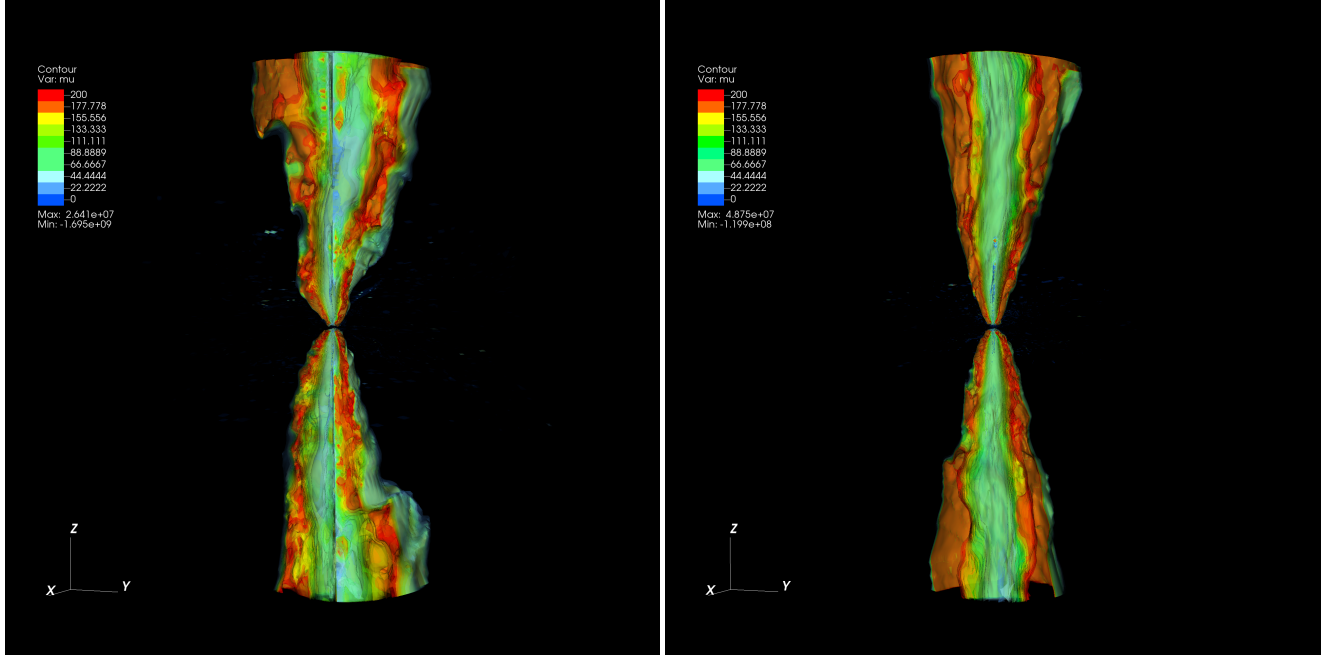


**Figure 7.** 3D jet structure at time  $t = 5000 t_g$  for (a) Fishbone-Moncrief (FM76) model (left panel) and (b) Chakrabarti (Ch85) model (right panel). The plots show the contours of the energetics parameter defined as  $\mu$  (see Equation 9) up to a radius of  $200 r_g$  in both directions. The plots are clipped along the YZ-plane to show the inner structure of the jet.

of the toroidal magnetic field component in the disk as described in section 3.1.

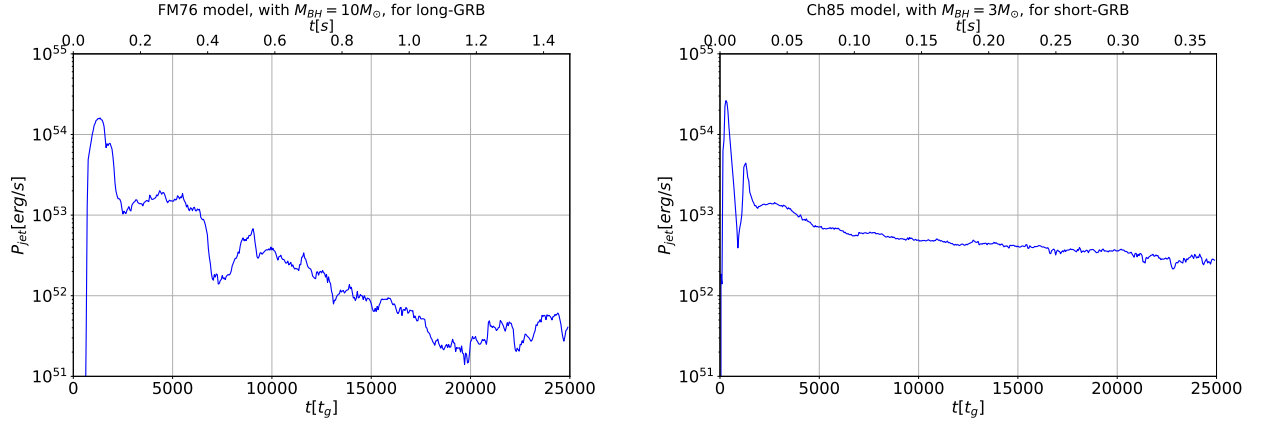
### 3.3.1. Variability of the jet and accretion rate

Figure 9 shows the variability of the jet energetics parameter with time as measured at the location 1, that is at the inner region closer to the axis of the jet, for our two models. We calculate the average duration of the peak widths at their half maximum and use it as a proxy for the minimum variability time scale (MTS) of the jet. The MTS computed from the above chosen locations and their averages are given in Table 2. The variability time scale has a smaller value in the inner

region of the jet for both the models and thus the peaks have shorter duration at smaller angles from the rotation axis of the black hole. To better understand the time variability of the jet emission we also computed the power density spectra (PDS) of the  $\mu$  variability data from these chosen locations. We fit this data to a power law function of the form  $y(x) = Ax^\alpha$  and calculate its slope. Figure 10 shows the PSD and the power law fit for the  $\mu$  data from both the locations, for our models. The slopes of the fitted power law curves are also given in Table 2.

### 3.3.2. Jet profile





**Figure 8.** Jet power estimated by the Blandford-Znajek luminosity (see Equation 10) in physical units (erg/s) as a function of time (in  $t_g$ ). We also show the physical timescales scaled with the assumed black hole masses of long and short GRBs: (a) with initial Fishbone-Moncrief configuration (FM76) and (b) with initial Chakrabarti configuration (Ch85).

Model	Lorentz factor ( $\Gamma$ )			MTS estimated (in $t_g$ )			Slope of the PDS	
	Location 1	Location 2	Average	Location 1	Location 2	Average	Location 1	Location 2
FM76	105.96	89.45	97.71	178.63	269.80	224.21	-0.8253	-1.4899
Ch85	61.33	202.36	131.85	147.01	147.72	147.37	-0.8016	-1.1310

**Table 2.** The values of the bulk Lorentz factor ( $\Gamma$ ), estimated minimum variability timescale (MTS) (in  $t_g$ ) and the slopes of the power law (PL) fit to the power density spectrum (PDS) plots, at the two chosen locations inside the jet for our models.

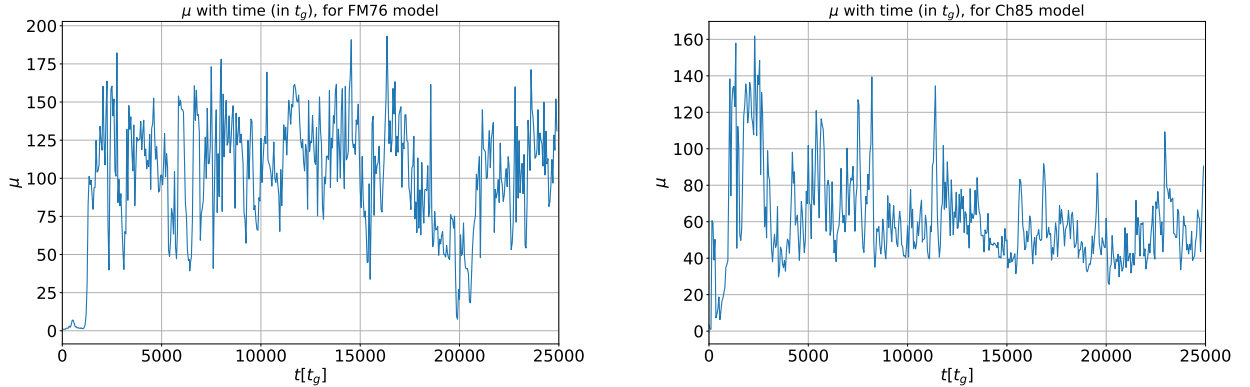


**Figure 9.** The time evolution of the jet energetics parameter  $\mu$  at a chosen location  $r = 150r_g$  and  $\theta = 5^\circ$  (location 1), averaged over the toroidal angle  $\phi$  for the models (a) with initial Fishbone-Moncrief configuration (FM76) and (b) with initial Chakrabarti configuration (Ch85).

Figure 7 shows the 3D distribution of the jet energetics parameter  $\mu$  for both of our models up to a radius of  $200r_g$  at a dynamical time  $5000t_g$ . These plots represent the evolved structure of the jet after a certain time after the jet has launched. Both of our models clearly produce structured jets rather than a simple top-hat, similar to what we have seen in our previous study with 2D simulations. But our current models evolve the non-axisymmetric structure of the jet. Larger values of Lorentz factor are obtained farther from the axis as can be seen from the plots. So the jets pro-

duced by our models have a comparatively hollow core, with small Lorentz factors ( $\sim 10$ ) up to an angle of  $\sim 5^\circ$ . Higher Lorentz factors are reached far from the axis the jet and it is faster along the edges. This is similar to those observed in previous simulations of MHD jets as described in Nathanail et al. (2020). Further description of the jet structure is provided in the next section where we discuss it in the context of short GRBs.

In order to qualitatively understand the energy distribution in the jet, we calculated the jet Lorentz factor as a function of

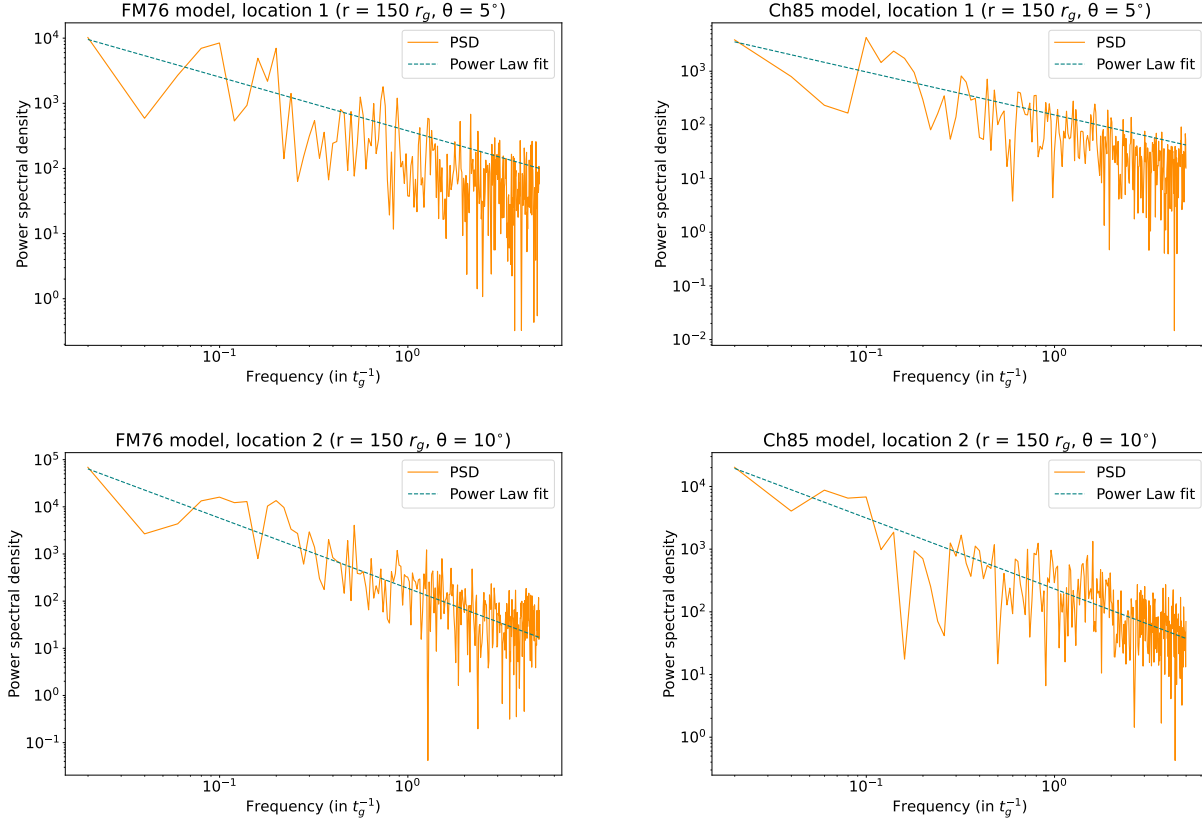


**Figure 10.** The power spectral density computed from the  $\mu$ -time variability data at the chosen locations 1 and 2 and the corresponding power law fit for the models (a) with initial Fishbone-Moncrief configuration (FM76) and (b) with initial Chakrabarti configuration (Ch85).

the polar angle at a very large distance from the center. Figure 11 shows the time averaged jet Lorentz factor estimated at a large distance ( $2000r_g$ ) as function of the polar angle for both the models. For the FM model, the most energetic parts of the jet is confined mostly within an angle of  $\sim 11-12^\circ$  and the highest Lorentz factors are reached around  $9^\circ$  from the axis. We discuss this model in the context of long GRBs. On the other hand, the model with Chakrabarti initial configuration, which we consider as the central engine for short GRBs, has a somewhat different jet profile. In this model, the jet does not clearly confine to an angle of  $\lesssim 15^\circ$  but instead spreads up to  $25^\circ$ . It is worth noting that the inner part near to the axis of rotation is much less energetic in this model. The outer regions of the jet, which is away from the rotational axis of the black hole, are also more structured in this model. The value of the Lorentz factor along different  $\phi$  slices vary significantly between each other.

### 3.4. Effect of the resolution and the initial magnetic field geometry in achieving the MAD state

The resolution study of White et al. (2019) was particularly focussing on the MAD scenario. They find that certain global properties converge with resolution such as the mass accretion rate, jet efficiency and the MRI suppression fac-

tor. We note that our global resolution of  $288 \times 256 \times 128$  is at least at the level of their level 2 resolution which satisfactorily resolves these quantities. Our models clearly suppress the MRI and result in a MAD state shortly after the beginning of the simulations. Following White et al. (2019) we assume that the accumulated flux on the horizon  $\phi_{BH}$  is not affected by the resolution. Thus we argue that the large scale structures of the MAD flows are correctly described by our models. Our models have sufficiently enough resolution to properly catch the base of the jet structure and Lorentz factor profiles as well.

We initialize our models with single large poloidal loops of magnetic field. Such configurations are proved to result in the development of strong poloidal flux in the vicinity of the black horizon as the accretion proceeds (McKinney et al. 2012; Penna et al. 2013). This helps in achieving the MAD state within a short time ( $\sim 1500-2000t_g$ ) after the simulation has begun (as can be seen from Fig. 6). We note, that some recent simulations have shown that the development of such strong poloidal flux happens even with much weaker initial fields (Liska et al. 2020) and also develops a magnetically arrested accretion disk state. In order to see such effects, we would need much higher resolutions and longer runs as compared to the ones presented in this pa-

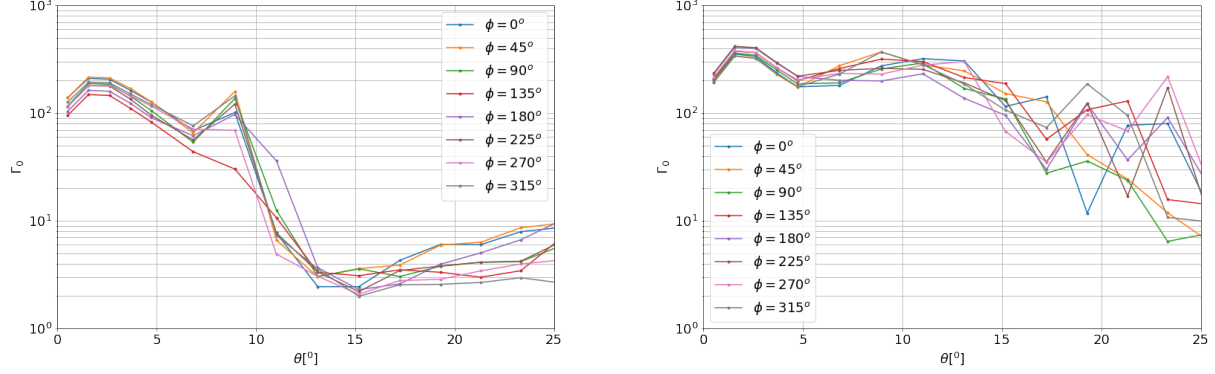


**Figure 11.** Time averaged jet Lorentz factor measured at a large distance of  $2000 r_g$ , as a function of the polar angle  $\theta$ . Figure shows the jet profile at different selected slices of  $\phi$  for the model with (a) Fishbone-Moncrief initial configuration (FM76) and (b) Chakrabarti initial configuration (Ch85).

per. However, some of our models, previously run in 2D, and for shorter amounts of time with weaker initial magnetic field configurations, also showed the building up of strong poloidal flux after a certain time (Janiuk et al. 2021).

#### 4. APPLICATION TO THE ENGINE MODELING OF SHORT AND LONG GRBS

##### 4.1. Comparison with previous models for GRBs

We use our CH85 model in the context of short GRBs, as a post-merger system in which an accretion disk has been formed. In a realistic scenario of a BNS system, the disrupted neutron star material is non-axisymmetric and composed of clumps of matter, with propagating shock waves (Foucart et al. 2014). Therefore, breaking the initial axisymmetry of the disk with the introduction of random perturbations in the  $\phi$ -direction is justified.

Proga & Zhang (2006) used their hyperaccretion models for GRBs at late times and proposed that the episodic energy output in the jets is connected with the changes in the mass supply driven by the accretion rate. They propose this as a model to explain the X-ray flares observed from the GRBs. They show with their chosen models that the energy release is repeatedly halted and restarted given the mass supply rate decreases with time which is the case in both binary merger and collapsar scenarios. This is similar to behaviour observed in our previous work Janiuk et al. (2021). In our current models there is no mass supply to the outer edge of the disk. The short episodic rise in the mass accretion rate in the initial stages is due to the dynamic nature of the magnetic field, and relaxation of the initial, stationary conditions, which was derived for a non-magnetized disk. After the initial condition is relaxed, i.e. around time  $5000 t_g$ , the variability of accretion rate driven by interchange instabilities developed in the plasma continues in the magnetically arrested disk. The jet power is also varying and its magnitude is slowly decreasing with time. This can be partly connected to the falling mass

accretion rate, which is decreasing at a slightly different rate. The rate of decrease of the jet power in both the models differs substantially. In the FM76 model it falls by three orders of magnitude as the simulation proceeds while in the Ch85 model it falls by two orders of magnitude. The differences can be connected to the varying strength of magnetic flux on the black hole horizon.

Lloyd-Ronning et al. (2019) put limits on the magnetic field strength and the black hole mass needed to power Blandford-Znajek jets from the observed luminosities of short and long GRBs. They assume a central engine with black hole mass in the range of  $0.5\text{--}4 M_\odot$  for the short GRBs and  $2\text{--}10 M_\odot$  for the long GRBs and they find that magnetic field strengths in the range of  $\sim 5 \times 10^{14}$  to up to  $\sim 10^{17} G$  (for the long GRBs) and  $\sim 10^{15}$  to  $\sim 10^{17} G$  (for the short GRBs) are needed to power the observed GRBs with the assumed mass of the central engine. The magnetic fields inferred from their analysis are extreme and in practice such fields can be generated and sustained only through special mechanisms. Generally, a small extant magnetic field in a disk can be amplified by the MRI. But, the MRI is suppressed in our simulations due to the magnetic arresting of the disk which is evident from the growth of magnetic flux at the black hole horizon. The magnetic field strength at the black hole horizon at an evolved time ( $5000 t_g$ ) in our long GRB model (FM76) is estimated as  $3.51 \times 10^{14} G$  and in our short GRB model (Ch85) it is  $7.74 \times 10^{14} G$ . This is in the range of previous estimations. Our simulations show that the disk can sustain such an amount of flux near the black hole horizon over time and presents such a configuration as a viable candidate for explaining the jet variability properties of the GRBs. For comparison, Kiuchi et al. (2014) evolve a high resolution BNS merger scenario. In their simulations magnetic field is amplified within multiple mechanisms including Kelvin-Helmholtz instability during the merger and MRI during post-merger evolution. They show it is possible

to have a highly magnetized disk with magnetic field stronger than  $10^{15.6}\text{G}$  over a big region of the disk.

Our FM76 model (model 1) is embedded in a poloidal magnetic field which follows the disk density structure with a dependence on the fifth power of radius. This analytic solution is a standard initial condition for a thick disk and the imposed magnetic field is in such a way that it takes a short amount of time to accrete more poloidal flux to the black hole horizon. We consider this model as a candidate for the central engine of long GRBs. On the other hand, we consider our Ch85 model (model 2) embedded in a poloidal magnetic field due to a circular current at the radius of pressure maximum of the disk as a candidate for the central engine of short GRBs. In this model, the imposed magnetic field is in such a way that it takes shorter time to develop more poloidal magnetic flux on the black horizon, which results in a magnetically arrested disk. At a later time of the simulation ( $t \sim 2500t_g$ ), the strength of the poloidal magnetic field at the inner region of the disk is  $B_z = 1.53 \times 10^{-3}$  for the FM76 model and  $B_z = 1.09 \times 10^{-3}$  for Ch85 model (in code units) which is comparable.

#### 4.2. Jet opening angles in short and long GRBs

Our numerical simulations can give a picture of the jet structure in the long and short GRBs based on the models we are considering for the two scenarios. The time averaged jet Lorentz factor profile with  $\theta$  gives information about where most of the energy in the jet is concentrated and the jet opening angles in our models. Based on their HD and MHD simulations [Nathanail et al. \(2020\)](#) focus particularly on the properties of GRB170817A. They observe a self consistent jet launching in their MHD simulations. Their MHD jets have a hollow core of up to  $\sim 4-5^\circ$  and the jets carry a significant amount of matter. When comparing to our models, we have a clearly hollow core up to an angle of  $5^\circ$  in our Ch85 model. On the other hand, the jet launched in our FM76 model has higher Lorentz factors closer to the axis as well, compared to the Ch85 model. But, in our FM76 model also, even higher Lorentz factors are reached at a significant angle ( $\theta \gtrsim 10^\circ$ ) from the axis. Compared to their models, the jets in both of our models do not contain any considerable amount of matter. This is apparent from the density plots on the top middle and right panels given in Figures 1 and 2.

[Margutti et al. \(2018\)](#) studied different models based on hydrodynamic simulations of the jet interaction with BNS ejecta to get the opening angle values from the GRB170817A afterglow observations. They show two representative scenarios for jet opening angles of  $5^\circ$  and  $15^\circ$  considering a top-hat structure for the jet, assuming off-axis viewing angles  $\theta_{obs} \sim 15^\circ - 25^\circ$ . But the top-hat jets viewed off-axis failed to reproduce the larger X-ray and radio luminosities in the early days after the prompt emission from the source

and also failed to account for the mild and steady rise of the non-thermal emission observed. So a simple top-hat structure is not a likely scenario for the afterglows of GW170817. Rather, a structured and collimated relativistic outflow is considered as the probable scenario for this observation, with the GRB assumed to be seen off-axis. Many other authors also support the scenario of a structured jet which is seen off-axis based on their models for this source. e.g. ([Kathirgamaraju et al. 2018](#)). If we assume the inference of [Margutti et al. \(2018\)](#) that the GRB170817A was a "classical" short GRB with a structured collimated jet and reached up to an energy of  $\sim 10^{50}$  erg which was observed off-axis to be correct, we can consider the jet structure described by their models. The jet produced in their representative models with this assumption, has a narrow ultra-relativistic core of  $\theta_c \sim 9^\circ$  with  $\Gamma \sim 100$  surrounded by a mildly relativistic sheath up to angle of  $\lesssim 60^\circ$ . In our models, the time averaged terminal Lorentz factor profile computed at  $\sim 2000r_g$  (shown in Figure 11) also clearly shows the existence of structured jets. The Ch85 model, which we consider as a candidate for a short GRB central engine, also shows a complex structured jet profile with no clearly defined core region when averaged over time. In this model, the jet is confined to a rather broader angle of  $\theta \lesssim 25^\circ$ . But, the jet produced in this model reaches the highest Lorentz factors at around an angle of  $\sim 9^\circ$  which is in coincidence with the value of narrow jet core in the models of [Margutti et al. \(2018\)](#). Figure 7 shows the internal sub-structure of the base of the jet from our simulations at a given time. Both these plots show the evolved non-axisymmetric structured nature of the jet. They also qualitatively depict the jet core with higher Lorentz factors ( $\sim 150 - 200$ ) at some certain angle away from the axis.

Another possible scenario, explaining why GRB 170817 is dimmer than a classical short GRB, is based on the fact that post-merger remnants are surrounded by high-speed, neutron-rich dynamical ejecta which produce heavy elements with high opacity through r-process nucleosynthesis. Therefore the emissions from inner parts can be partially masked by outer opaque material [Kasen et al. \(2015\)](#). GRB 080503 is another example of a faint GRB, accompanied by an extremely bright extended prompt X-ray emission. The faintness of this GRB can be explained by off-axis jet similar to GRB170817 ([Perley et al. 2009](#); [Fong et al. 2015](#)).

[Fong et al. \(2015\)](#) considered 11 short GRB events with equal weighting (see their Table 5) and calculated the jet opening angles by giving Gaussian probability distributions to the measurements they considered. Employing a realistic upper bound of  $\theta_{j,max} = 30^\circ$  on the opening angles (obtained from the previously available post-merger black hole accretion simulations), they obtain a median value of  $\langle \theta_j \rangle = 16 \pm 10$  degrees. The jet from our Ch85 model has a value which tend towards the upper limit of this value. In the FM76



model we have a structured jet with most of the energetic part confined to  $\theta \sim 11 - 12^\circ$ . The profile for this model shows an ultra-relativistic core with  $\Gamma \sim 100$  peaking around  $\theta_c \sim 9^\circ$ . Fong et al. (2015) also compute the jet opening angles for the long GRBs from the measurements of 248 samples and find a median value of  $\langle \theta_j \rangle = 13^{+5}_0$  degrees. The value of  $11^\circ$  obtained from our FM76 model matches with the lower bound of the estimated value from the observations.

#### 4.3. Jet variability timescale in short and long GRBs

When we consider our model with Chakrabarti initial torus (Ch85) as a plausible central engine for the short GRBs, we can use a black hole mass of  $3 M_\odot$  to scale the physical quantities and compute the minimum variability time in seconds. We get an average value of  $147.37 t_g$  for the minimum variability timescale from two chosen locations along the jet direction for this model. This scales to a value of 2.178 ms in physical units. Similarly when we consider our FM76 model as a collapsar remnant disk and use a value of  $10 M_\odot$  for the central black hole, we can estimate the resulting minimum variability timescale. We get an average value of  $224.21 t_g$  for the minimum variability timescale in code units from this model which gives a value of 13.257 ms in physical units. MacLachlan et al. (2013) present a wavelet analysis using a collection of observed samples from the FERMI data to show that the variability timescales of the short and long GRBs differ from each other. In their study, they find a marginal positive correlation between the minimum variability timescale and burst duration for both classes of bursts. The lowest variability timescale from their study is 3 ms. Our results are in agreement with these observations.

Golkhou et al. (2015) put constraints on the minimum variability timescales for the GRBs observed by the FERMI/GBM instrument. They find the median minimum timescale for long GRBs as 45 ms and for the short GRBs as 10 ms. Only less than 10% of their selected samples show variability smaller than 2 ms and this requires Lorentz factors higher than 400. The minimum variability timescales obtained from our models are in the lowest range of these observed values.

The power density spectra (PDS) computed for our models also reveal information about the time variability data. The variability of the energy blobs ejected close to the inner regions of the jet in both models have a smaller PDS slope as compared to the variability measured at the outer region for the fitted power law. So, in general, the outer wall of the jet shows higher variability as compared to the inner part closer to the jet axis. Also, the PL fit for the long GRB model has steeper slope as compared to the short GRB model at both the locations in which the variability is measured. The slope ( $\alpha$ ) values are in the range but smaller than  $5/3$  which is predicted by the turbulence model (Beloborodov et al. 2000). More re-

cent observational studies give PDS slope values, with a PL fit, in the range 1.347 to 2.874 (Guidorzi et al. 2016) and 1.42 to 4.95 (Dichiara et al. 2016) for the long GRBs and in the range 1.398 to 2.507 (Dichiara et al. 2013) for the short GRBs. Our results of the jet variability measured at the outer part are consistent with the lower limit of the observed PDS slopes.

Sonbas et al. (2015) find an anti-correlation between the minimum variability timescale and the bulk Lorentz factor for the GRB samples they considered from the SWIFT and FERMI data. We have not calculate sufficient number of models to do a parameter study for obtaining a correlation between the variability timescale and Lorentz factor. But our models do systematically give smaller minimum variability timescales for higher Lorentz factors from our two models and also from different regions of the jet.

## 5. CONCLUSIONS

We have done 3-dimensional GRMHD simulations of the accretion disk around a Kerr black hole considering two different initial analytical equilibrium solutions. The Chakrabarti initial solution has an angular momentum distribution constant over specific surfaces and changes with the radius rather than being constant over the entire disk. This arguably gives a more realistic scenario as compared to the initial FM solution. These solutions are imposed upon by poloidal magnetic fields which results in magnetic turbulence and MRI which initially drives the accretion. As the accretion proceeds the plasma brings more magnetic flux to the black hole horizon and results in a magnetic arrested accretion state which prevents further falling of matter into the black hole. We consider the MAD state as the plausible central engine of GRBs and investigate its effect on the time variability properties and the structure of the ejected jet. Our models self consistently produce structured jets with a relatively hollow core, up to an angle of  $\sim 5^\circ$ , and higher Lorentz factors are reached on the edges of the jets. The two initial models and the imposed magnetic field geometry affect the jet structure which is evident from the different profiles and internal structures of the jets. The models give a jet opening angle of  $\sim 11^\circ$  and  $\sim 25^\circ$  respectively for the short and long GRBs, which is consistent with the observations. Also the minimum variability timescale is computed for both of our models and they are found to be in the lower range of variability timescale from observations. Finally, the PDS spectral slopes are somewhat flatter than the classical  $\alpha = 5/3$  slope, but within the observed range.

1 This research was supported in part by the grant DEC-  
 2 2019/35/B/ST9/04000 from the Polish National Science  
 3 Center. This research was carried out with the support of  
 4 the Interdisciplinary Center for Mathematical and Compu-  
 5 tational Modeling at the University of Warsaw (ICM UW)  
 6 under the grant numbers g85-986 and g86-987.  
 7 *Software:* Matplotlib (Hunter 2007), NumPy (Har-  
 8 ris et al. 2020), SciPy (Virtanen et al. 2020) and VisIt  
 9 (Childs et al. 2012).

## REFERENCES

- Abbott, B. P., et al. 2017, *PhRvL*, 119, 161101, doi: [10.1103/PhysRevLett.119.161101](https://doi.org/10.1103/PhysRevLett.119.161101)
- Abramowicz, M. A., & Fragile, P. C. 2013, *Living Reviews in Relativity*, 16, 1, doi: [10.12942/lrr-2013-1](https://doi.org/10.12942/lrr-2013-1)
- Balbus, S. A., & Hawley, J. F. 1991, *ApJ*, 376, 214, doi: [10.1086/170270](https://doi.org/10.1086/170270)
- Beloborodov, A. M., Stern, B. E., & Svensson, R. 2000, *ApJ*, 535, 158, doi: [10.1086/308836](https://doi.org/10.1086/308836)
- Blandford, R. D., & Znajek, R. L. 1977, *MNRAS*, 179, 433, doi: [10.1093/mnras/179.3.433](https://doi.org/10.1093/mnras/179.3.433)
- Boyer, R. H., & Lindquist, R. W. 1967, *Journal of Mathematical Physics*, 8, 265, doi: [10.1063/1.1705193](https://doi.org/10.1063/1.1705193)
- Burrows, A., Dessart, L., Livne, E., Ott, C. D., & Murphy, J. 2007, *ApJ*, 664, 416, doi: [10.1086/519161](https://doi.org/10.1086/519161)
- Chael, A., Narayan, R., & Johnson, M. D. 2019, *MNRAS*, 486, 2873, doi: [10.1093/mnras/stz988](https://doi.org/10.1093/mnras/stz988)
- Chakrabarti, S. K. 1985, *ApJ*, 288, 1, doi: [10.1086/162755](https://doi.org/10.1086/162755)
- Childs, H., Brugger, E., Whitlock, B., et al. 2012, in *High Performance Visualization—Enabling Extreme-Scale Scientific Insight* (CRC Press), 357–372
- Di Matteo, T., Perna, R., & Narayan, R. 2002, *Astrophys. J.*, 579, 706, doi: [10.1086/342832](https://doi.org/10.1086/342832)
- Dichiara, S., Guidorzi, C., Amati, L., Frontera, F., & Margutti, R. 2016, *A&A*, 589, A97, doi: [10.1051/0004-6361/201527635](https://doi.org/10.1051/0004-6361/201527635)
- Dichiara, S., Guidorzi, C., Frontera, F., & Amati, L. 2013, *ApJ*, 777, 132, doi: [10.1088/0004-637X/777/2/132](https://doi.org/10.1088/0004-637X/777/2/132)
- Duez, M. D. 2010, *Classical and Quantum Gravity*, 27, 114002, doi: [10.1088/0264-9381/27/11/114002](https://doi.org/10.1088/0264-9381/27/11/114002)
- Fishbone, L. G., & Moncrief, V. 1976, *ApJ*, 207, 962, doi: [10.1086/154565](https://doi.org/10.1086/154565)
- Fong, W., Berger, E., Margutti, R., & Zauderer, B. A. 2015, *ApJ*, 815, 102, doi: [10.1088/0004-637X/815/2/102](https://doi.org/10.1088/0004-637X/815/2/102)
- Foucart, F., Deaton, M. B., Duez, M. D., et al. 2014, *PhRvD*, 90, 024026, doi: [10.1103/PhysRevD.90.024026](https://doi.org/10.1103/PhysRevD.90.024026)
- Galama, T. J., Vreeswijk, P. M., van Paradijs, J., et al. 1999, *A&AS*, 138, 465, doi: [10.1051/aas:1999311](https://doi.org/10.1051/aas:1999311)
- Gammie, C. F., McKinney, J. C., & Tóth, G. 2003, *ApJ*, 589, 444, doi: [10.1086/374594](https://doi.org/10.1086/374594)
- Gammie, C. F., Shapiro, S. L., & McKinney, J. C. 2004, *ApJ*, 602, 312, doi: [10.1086/380996](https://doi.org/10.1086/380996)
- Golkhou, V. Z., Butler, N. R., & Littlejohns, O. M. 2015, *ApJ*, 811, 93, doi: [10.1088/0004-637X/811/2/93](https://doi.org/10.1088/0004-637X/811/2/93)
- Guidorzi, C., Dichiara, S., & Amati, L. 2016, *A&A*, 589, A98, doi: [10.1051/0004-6361/201527642](https://doi.org/10.1051/0004-6361/201527642)
- Harris, C. R., Millman, K. J., van der Walt, S. J., et al. 2020, *Nature*, 585, 357, doi: [10.1038/s41586-020-2649-2](https://doi.org/10.1038/s41586-020-2649-2)
- Hunter, J. D. 2007, *Computing in Science & Engineering*, 9, 90, doi: [10.1109/MCSE.2007.55](https://doi.org/10.1109/MCSE.2007.55)
- Igumenshchev, I. V. 2008, *ApJ*, 677, 317, doi: [10.1086/529025](https://doi.org/10.1086/529025)
- Jackson, J. D. 1998, *Classical Electrodynamics*, 3rd Edition (John Wiley)
- Janiuk, A., James, B., & Palit, I. 2021, *ApJ*, 917, 102, doi: [10.3847/1538-4357/ac0624](https://doi.org/10.3847/1538-4357/ac0624)
- Janiuk, A., Perna, R., Di Matteo, T., & Czerny, B. 2004, *Mon. Not. Roy. Astron. Soc.*, 355, 950, doi: [10.1111/j.1365-2966.2004.08377.x](https://doi.org/10.1111/j.1365-2966.2004.08377.x)
- Jaroszynski, M. 1996, *Astron. Astrophys.*, 305, 839, <https://arxiv.org/abs/astro-ph/9506062>
- Just, O., Obergaulinger, M., Janka, H. T., Bauswein, A., & Schwarz, N. 2016, *ApJL*, 816, L30, doi: [10.3847/2041-8205/816/2/L30](https://doi.org/10.3847/2041-8205/816/2/L30)
- Kasen, D., Fernández, R., & Metzger, B. D. 2015, *MNRAS*, 450, 1777, doi: [10.1093/mnras/stv721](https://doi.org/10.1093/mnras/stv721)
- Kathirgamaraju, A., Barniol Duran, R., & Giannios, D. 2018, *MNRAS*, 473, L121, doi: [10.1093/mnras/slx175](https://doi.org/10.1093/mnras/slx175)
- Kiuchi, K., Kyutoku, K., Sekiguchi, Y., Shibata, M., & Wada, T. 2014, *PhRvD*, 90, 041502, doi: [10.1103/PhysRevD.90.041502](https://doi.org/10.1103/PhysRevD.90.041502)
- Kouveliotou, C., Meegan, C. A., Fishman, G. J., et al. 1993, *ApJL*, 413, L101, doi: [10.1086/186969](https://doi.org/10.1086/186969)
- Li, L.-X. 2000, *ApJL*, 531, L111, doi: [10.1086/312538](https://doi.org/10.1086/312538)
- Liska, M., Tchekhovskoy, A., & Quataert, E. 2020, *MNRAS*, 494, 3656, doi: [10.1093/mnras/staa955](https://doi.org/10.1093/mnras/staa955)

- Liu, T., Gu, W.-M., & Zhang, B. 2017, *NewAR*, 79, 1, doi: [10.1016/j.newar.2017.07.001](https://doi.org/10.1016/j.newar.2017.07.001)
- Lloyd-Ronning, N. M., Dolence, J. C., & Fryer, C. L. 2016, *MNRAS*, 461, 1045, doi: [10.1093/mnras/stw1366](https://doi.org/10.1093/mnras/stw1366)
- Lloyd-Ronning, N. M., Fryer, C., Miller, J. M., et al. 2019, *MNRAS*, 485, 203, doi: [10.1093/mnras/stz390](https://doi.org/10.1093/mnras/stz390)
- MacLachlan, G. A., Shenoy, A., Sonbas, E., et al. 2013, *MNRAS*, 432, 857, doi: [10.1093/mnras/stt241](https://doi.org/10.1093/mnras/stt241)
- Margutti, R., & Chornock, R. 2021, *ARA&A*, 59, doi: [10.1146/annurev-astro-112420-030742](https://doi.org/10.1146/annurev-astro-112420-030742)
- Margutti, R., Alexander, K. D., Xie, X., et al. 2018, *ApJL*, 856, L18, doi: [10.3847/2041-8213/aab2ad](https://doi.org/10.3847/2041-8213/aab2ad)
- McKinney, J. C., & Gammie, C. F. 2004, *ApJ*, 611, 977, doi: [10.1086/422244](https://doi.org/10.1086/422244)
- McKinney, J. C., Tchekhovskoy, A., & Blandford, R. D. 2012, *MNRAS*, 423, 3083, doi: [10.1111/j.1365-2966.2012.21074.x](https://doi.org/10.1111/j.1365-2966.2012.21074.x)
- Mizuta, A., Ebisuzaki, T., Tajima, T., & Nagataki, S. 2018, *MNRAS*, 479, 2534, doi: [10.1093/mnras/sty1453](https://doi.org/10.1093/mnras/sty1453)
- Narayan, R., Chael, A., Chatterjee, K., Ricarte, A., & Curd, B. 2021, arXiv e-prints, arXiv:2108.12380. <https://arxiv.org/abs/2108.12380>
- Narayan, R., Igumenshchev, I. V., & Abramowicz, M. A. 2003, *PASJ*, 55, L69, doi: [10.1093/pasj/55.6.L69](https://doi.org/10.1093/pasj/55.6.L69)
- Nathanail, A., Gill, R., Porth, O., Fromm, C. M., & Rezzolla, L. 2020, *MNRAS*, 495, 3780, doi: [10.1093/mnras/staa1454](https://doi.org/10.1093/mnras/staa1454)
- Noble, S. C., Gammie, C. F., McKinney, J. C., & Del Zanna, L. 2006, *ApJ*, 641, 626, doi: [10.1086/500349](https://doi.org/10.1086/500349)
- Paczynski, B. 1991, *Acta Astronomica*, 41, 257
- Paschalidis, V., Etienne, Z. B., & Shapiro, S. L. 2013, *PhRvD*, 88, 021504, doi: [10.1103/PhysRevD.88.021504](https://doi.org/10.1103/PhysRevD.88.021504)
- Penna, R. F., Narayan, R., & Sądowski, A. 2013, *MNRAS*, 436, 3741, doi: [10.1093/mnras/stt1860](https://doi.org/10.1093/mnras/stt1860)
- Perego, A., Yasin, H., & Arcones, A. 2017, *Journal of Physics G Nuclear Physics*, 44, 084007, doi: [10.1088/1361-6471/aa7bdc](https://doi.org/10.1088/1361-6471/aa7bdc)
- Perley, D. A., Metzger, B. D., Granot, J., et al. 2009, *The Astrophysical Journal*, 696, 1871, doi: [10.1088/0004-637x/696/2/1871](https://doi.org/10.1088/0004-637x/696/2/1871)
- Piran, T. 2004, *Reviews of Modern Physics*, 76, 1143, doi: [10.1103/RevModPhys.76.1143](https://doi.org/10.1103/RevModPhys.76.1143)
- Popham, R., Woosley, S. E., & Fryer, C. 1999, *Astrophys. J.*, 518, 356, doi: [10.1086/307259](https://doi.org/10.1086/307259)
- Proga, D., & Zhang, B. 2006, *MNRAS*, 370, L61, doi: [10.1111/j.1745-3933.2006.00189.x](https://doi.org/10.1111/j.1745-3933.2006.00189.x)
- Rezzolla, L., Giacomazzo, B., Baiotti, L., et al. 2011, *ApJL*, 732, L6, doi: [10.1088/2041-8205/732/1/L6](https://doi.org/10.1088/2041-8205/732/1/L6)
- Richers, S., Kasen, D., O'Connor, E., & Fernandez, R. and Ñ, C. D. 2015, *ApJ*, 813, 38, doi: [10.1088/0004-637X/813/1/38](https://doi.org/10.1088/0004-637X/813/1/38)
- Ruiz, M., Tsokaros, A., & Shapiro, S. L. 2020, *PhRvD*, 101, 064042, doi: [10.1103/PhysRevD.101.064042](https://doi.org/10.1103/PhysRevD.101.064042)
- Sapountzis, K., & Janiuk, A. 2019, *ApJ*, 873, 12, doi: [10.3847/1538-4357/ab0107](https://doi.org/10.3847/1538-4357/ab0107)
- Sharma, V., Iyyani, S., & Bhattacharya, D. 2021, *ApJL*, 908, L2, doi: [10.3847/2041-8213/abd53f](https://doi.org/10.3847/2041-8213/abd53f)
- Sonbas, E., MacLachlan, G. A., Dhuga, K. S., et al. 2015, *ApJ*, 805, 86, doi: [10.1088/0004-637X/805/2/86](https://doi.org/10.1088/0004-637X/805/2/86)
- Tchekhovskoy, A., Narayan, R., & McKinney, J. C. 2011, *MNRAS*, 418, L79, doi: [10.1111/j.1745-3933.2011.01147.x](https://doi.org/10.1111/j.1745-3933.2011.01147.x)
- Virtanen, P., Gommers, R., Oliphant, T. E., et al. 2020, *Nature Methods*, 17, 261, doi: [10.1038/s41592-019-0686-2](https://doi.org/10.1038/s41592-019-0686-2)
- Visser, M. 2007, arXiv e-prints, arXiv:0706.0622. <https://arxiv.org/abs/0706.0622>
- Vlahakis, N., & Königl, A. 2003, *ApJ*, 596, 1080, doi: [10.1086/378226](https://doi.org/10.1086/378226)
- Weinberg, S. 1972, *Gravitation and Cosmology: Principles and Applications of the General Theory of Relativity* (New York: Wiley)
- White, C. J., Stone, J. M., & Quataert, E. 2019, *ApJ*, 874, 168, doi: [10.3847/1538-4357/ab0c0c](https://doi.org/10.3847/1538-4357/ab0c0c)
- Woosley, S. E. 1993, *ApJ*, 405, 273, doi: [10.1086/172359](https://doi.org/10.1086/172359)